

Antiferromagnetic real-space configuration probed by dichroism in scattered x-ray beams with orbital angular momentum

Margaret R. McCarter¹, Ahmad I. U. Saleheen¹, Arnab Singh², Ryan Tumbleson^{1,3}, Justin S. Woods^{4,5}, Anton S. Tremsin⁶, Andreas Scholl¹, Lance E. De Long⁴, J. Todd Hastings⁷, Sophie A. Morley¹, and Sujoy Roy^{1,*}

¹*Advanced Light Source, Lawrence Berkeley National Laboratory, Berkeley, California 94720, USA*

²*Materials Science Division, Lawrence Berkeley National Laboratory, Berkeley, California 94720, USA*

³*Department of Physics, University of California, Santa Cruz, California 95064, USA*

⁴*Department of Physics and Astronomy, University of Kentucky, Lexington, Kentucky 40506, USA*

⁵*Materials Science Division, Argonne National Laboratory, Lemont, Illinois 60439, USA*

⁶*Space Sciences Laboratory, University of California, Berkeley, California 94720, USA*

⁷*Department of Electrical and Computer Engineering, University of Kentucky, Lexington, Kentucky 40506, USA*

 (Received 13 May 2022; revised 7 September 2022; accepted 11 January 2023; published 15 February 2023)

X-ray beams with orbital angular momentum (OAM) are a promising tool for x-ray characterization techniques. Beams with OAM have a helicity—an azimuthally varying phase—which leads to a gradient of the light field. New material properties can be probed by utilizing the helicity of an OAM beam. Here, we demonstrate a dichroic effect in resonant diffraction from an artificial antiferromagnet with a topological defect. We found that the scattered OAM beam has circular dichroism at the antiferromagnetic Bragg peak whose sign is coupled to its helicity, which reveals the real-space configuration of the antiferromagnetic ground state. Thermal cycling of the artificial antiferromagnet can change the ground state, as indicated by reversal of the sign of circular dichroism. This result is one of the first demonstrations of a soft x-ray spectroscopy characterization technique utilizing the OAM of x rays. This helicity-dependent circular dichroism exemplifies the potential to utilize OAM beams to probe matter in a way that is inaccessible using currently available x-ray techniques.

DOI: [10.1103/PhysRevB.107.L060407](https://doi.org/10.1103/PhysRevB.107.L060407)

X-ray–matter interactions are central to advanced characterization techniques such as x-ray absorption spectroscopy (XAS) and resonant x-ray scattering (RXS), which have transformed our understanding of magnetic, electronic, and orbital ordering phenomena in materials. Typically, these measurements involve varying the incident x-ray energy and polarization, giving rise to element-specific resonances that enhance signals from magnetic and orbital ordering and dichroic effects. These sensitive techniques can reveal non-trivial spin textures or nano-ordered phases that are difficult to probe with other methods. Some examples include multipolar order [1–5], charge ordering in high-temperature superconductors [6], and ordering in strongly correlated electron systems [7,8] and other quantum materials [9,10].

Quantum materials such as topological insulators, antiferromagnets, and complex oxides are increasingly explored for technological applications. Antiferromagnets are particularly interesting for spintronic applications. Due to the antiparallel spin arrangement of the two sublattices, antiferromagnets have net zero magnetization. They have no stray magnetic field, can be used at high frequencies, and are not easily susceptible to external magnetic fields. Ferromagnetic materials can be easily studied with x rays, due to their magnetization that leads to x-ray magnetic circular dichroism (XMCD) in

XAS. However, the absence of net magnetization in an antiferromagnet usually leads to zero XMCD, except in the special case of chiral spin textures [11–14].

Scattering techniques then are one of the most direct ways of measuring the staggered moments of an antiferromagnet. Collinear antiferromagnets can be studied using linear dichroism that occurs in XAS and RXS. Furthermore, the azimuthal angle or polarization dependence of RXS can identify domains in antiferromagnets with spin spirals [5,15–19] or chiral order [20]. In general, however, no techniques exist to directly probe the real-space, ground-state configuration or sublattice specific magnetization in an antiferromagnet.

A possible route to advance these techniques is by discovering a new kind of dichroism that takes advantage of the orbital angular momentum (OAM) of x rays. Here, we show how OAM beams created through RXS can distinguish between the two degenerate ground states of an artificial antiferromagnetic lattice with a topological defect. Right- and left-circularly polarized x-rays scatter differently from the antiferromagnet, and the resultant dichroism differs depending on the magnetic configuration as well as the helicity of the OAM beam that is produced. The observation of helicity-dependent circular dichroism demonstrates the potential for unique light-matter interactions involving OAM beams. This could lead to novel ways to probe materials via interactions of magnetic spins with the helicity of x-ray OAM beams.

OAM is a property of light beams where the wave front forms a helix along the propagation direction, and the phase

*sroy@lbl.gov

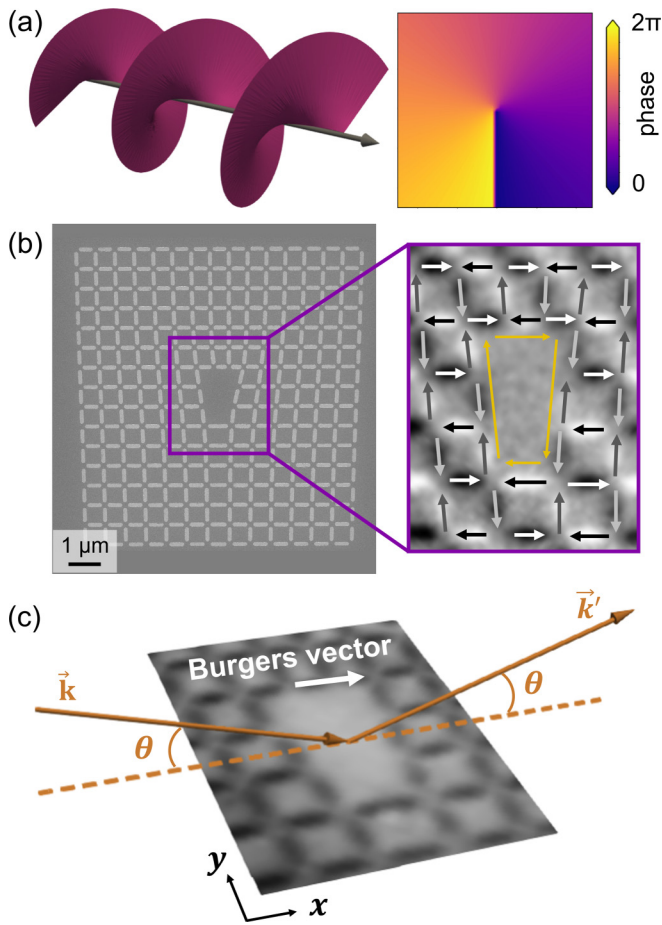


FIG. 1. Experiment details. (a) Left: Helical phase front of a beam carrying OAM with topological charge $\ell = +1$. The helix represents a surface of constant phase. Right: The cross section through an OAM beam has a phase that varies azimuthally. (b) SEM image of an artificial antiferromagnet with a \mathbb{Z}_2 topological defect (left), and XMCD PEEM (right) showing the antiferromagnetic configuration around the defect. The yellow arrows show the net magnetization direction around the defect. (c) Geometry for resonant scattering.

varies azimuthally, as shown in Fig. 1(a). The direction of the phase progression (counterclockwise or clockwise) determines the helicity (positive or negative) of the OAM beam. Beams with OAM have already found practical uses in the optical wavelength regime, such as optical tweezers and sub-wavelength imaging [21–27], and the potential exists for future applications in optical communications and quantum optics [21–24,28].

However, exploitation of OAM in x-ray beams is a relatively novel field [29–36], and the interaction between x rays carrying OAM and matter has only recently been studied experimentally [32,37]. Potential applications include x-ray holography [30,31], ptychography [36], and microscopy [38].

The electric field gradient of OAM beams could lead to new dichroic effects in XAS, such as enhanced sensitivity to quadrupolar transitions [39–41] and molecular chirality [32,42]. Dichroic effects due to the OAM of light have been observed in extreme ultraviolet resonant scattering [43], XAS of chiral molecules [32], and the photoelectric effect [44,45].

Analogous to circular dichroism (which is based on the differential absorption of right- or left-circularly polarized light), helicoidal dichroism is a new type of dichroism utilizing the differential absorption or scattering of OAM beams with positive or negative helicity. Additionally, because OAM beams have nontrivial topology, they could be used to characterize magnetic skyrmions [30], vortices [43,46], or other topological textures [33]. While theoretical predictions have been made [39,42], experimental verification of the spectroscopic applications of x-ray OAM beams is very limited [32].

One method to generate x-ray beams with OAM is to use an artificial antiferromagnet with a built-in topological defect [34]. An artificial antiferromagnet can be created by fabricating a square array of dipole-coupled nanomagnets. The nanomagnets are rectangular, so their strong shape anisotropy constrains the magnetization to align with the long axis, thereby creating an analog of an Ising system. Due to the asymmetric interaction between nearest neighbors, the system exhibits an antiferromagnetic ground state. Artificial antiferromagnets are widely studied as artificial spin ice systems [47,48], for understanding thermal fluctuations in metamaterials [49–53], and as candidates for magnonics applications [53–55].

RXS from such nanoarrays gives rise to magnetic diffraction [34,52,56,57]. In a previous study, it was shown that x rays with OAM are created when diffracted from an artificial antiferromagnetic lattice with a topological edge defect [34]. Interaction with the defect imparts its topology to the beam. This leads to scattered beams with OAM related to the defect’s topological charge, which can be directly observed using interference effects [34]. In this study we show that in addition to the OAM quantum number information, the antiferromagnetic Bragg peaks exhibit a helicity-dependent circular dichroism that can be utilized to determine the real-space, ground-state configuration of the artificial antiferromagnet.

An edge defect in a lattice can be characterized by its topological charge \mathbb{Z} , equal to the number of edge dislocations. We fabricated \mathbb{Z}_2 artificial antiferromagnetic lattices (with topological charge of 2) using electron-beam lithography and liftoff on ferromagnetic permalloy ($\text{Fe}_{0.8}\text{Ni}_{0.2}$) [58]. Real-space imaging was done using scanning electron microscopy (SEM), as seen in Fig. 1(b). The defect can be quantified by the Burgers vector $\vec{r} = 2a\hat{x}$, with \hat{x} defined along the direction of the edge dislocations.

Photoemission electron microscopy (PEEM) with XMCD was used to investigate the antiferromagnetic state. The beam energy was tuned to the Fe L_3 edge (707.6 eV) to obtain magnetic contrast. Images were taken for right- and left-circularly polarized x rays incident along the $[-1, 1]$ direction [58]. An XMCD image is created by taking the difference between images for opposite polarizations, resulting in bright and dark islands, as seen in Fig. 1(b). Bright and dark islands have a component of magnetization parallel or antiparallel, respectively, to the in-plane direction of the x rays. This information can be used to extract the magnetic configuration [58].

Since the magnetic lattice spacing is twice that of the structural lattice, the magnetic configuration effectively has one edge dislocation with a topological charge $\mathbb{Z}_m = \pm 1$, which depends on the magnetization surrounding the defect. Thus, our sample array contains a structural and magnetic defect

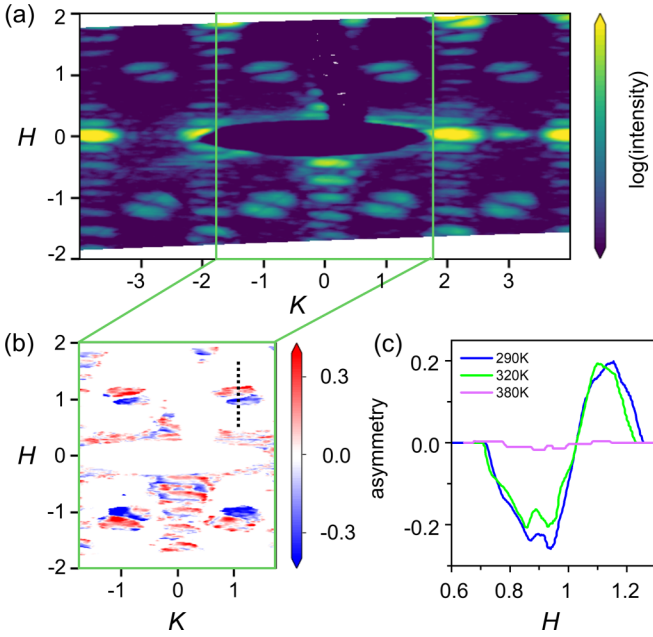


FIG. 2. Resonant x-ray scattering from an artificial antiferromagnet. (a) Sum of diffraction patterns for right- and left-circular polarizations. (b) Circular asymmetry occurs at the peaks. Red/blue corresponds to positive/negative values. (c) Temperature-dependent circular asymmetry measured along the line marked in (b). The asymmetry disappears upon heating above the antiferromagnetic transition temperature.

with different topological charge. We define the magnetic configuration in Fig. 1(b) as the $\mathbb{Z}_m = +1$ defect, with net clockwise magnetization surrounding the defect.

We have characterized the antiferromagnet using coherent RXS at the Fe L_3 edge with the scattering geometry shown in Fig. 1(c). The Burgers vector was parallel to the in-plane direction of the incident x-ray beam (the \hat{x} direction). The incident beam was a typical Gaussian x-ray beam used for scattering experiments (without OAM). The lattice gives rise to a diffraction pattern with peaks from the structural and magnetic lattices. Structural peaks appear at (H, K) when H and K are even integers, whereas magnetic peaks appear when H and K are odd integers. This is because the periodicity of the antiferromagnetic lattice is twice that of the structural lattice. Any peak with a component of its scattering vector parallel to the Burgers vector (i.e., any peak with $H \neq 0$) will have a nonzero OAM [34], whose value is $\ell\hbar$, where ℓ is equal to the diffraction peak order H .

The diffraction pattern in Fig. 2(a) is the sum of scattering for right- and left-circularly polarized incident x rays. The pattern has magnetic peaks at $H = \pm 1$ and structural peaks at $H = 0$. The magnetic peaks have OAM, leading to characteristic peaks with a central dark spot due to the phase singularity. The structural peaks at $H = 0$ have no OAM, because the scattering is perpendicular to the Burgers vector. Additionally, the scattering vector is related to the helicity of the beam. The peaks at $H = +1$ have OAM values $\ell = +1$, meaning it has positive helicity and the phase wraps counter-clockwise as seen in Fig. 1(a). On the other hand, peaks at $H = -1$ have OAM values $\ell = -1$, meaning that it has nega-

tive helicity and the phase wraps clockwise. It was previously shown [34] that the magnetic diffraction peaks from the \mathbb{Z}_2 lattice differ for right- versus left-circularly polarized incident x rays, but the spectroscopic power of this measurement was not yet determined. While dichroism was observed, it was not realized that it is related to the helicity of the outgoing OAM beam and the specific magnetic sublattice ordering. The dichroism can be quantified by the circular asymmetry:

$$\text{asymmetry} = \frac{I_{rc} - I_{lc}}{I_{rc} + I_{lc}}, \quad (1)$$

where I_{rc} and I_{lc} are the scattered intensities for right- and left-circularly polarized x rays. The sign of the asymmetry has a distinct pattern, as shown in Fig. 2(b), which is related to the helicity of the OAM beam. The asymmetry is half positive and half negative at each peak, so it switches sign when the phase changes by π . The asymmetry pattern also reverses sign upon changing from $H = +1$ to $H = -1$. The dichroism is then linked to the helicity of the beam, since changing from $H = +1$ to $H = -1$ also changes the OAM from $\ell = +1$ to $\ell = -1$.

For $H = +1$ peaks, the asymmetry implies that the right- (left-) circularly polarized x rays scatter with higher intensity to the top (bottom) half of the diffracted beam. In other words, the x rays and their interaction with the material's spin degree of freedom scatter circularly polarized light in a way that depends on the helicity of the scattered beam. We note that for a defect-free antiferromagnet, right- and left-circularly polarized Gaussian beams should scatter with the same intensity at the antiferromagnetic Bragg peaks [58]. This is why antiferromagnets do not usually give rise to circular dichroism.

Since $H = \pm 1$ peaks arise due to the antiferromagnetic ordering, the peaks and dichroism should disappear above the antiferromagnetic Ising transition temperature, which is $T_N \approx 380$ K for this artificial antiferromagnet [34]. To confirm this, we performed temperature-dependent measurements, as shown in Fig. 2(c). At room temperature, a line profile through an $H = +1$ peak clearly shows the half-positive, half-negative dichroism distribution. This persists to at least 320 K. At 380 K, there is no longer any dichroism, confirming that the peaks and dichroism disappear once the antiferromagnetic state is suppressed by thermal fluctuations.

To investigate how RXS can be used to distinguish between the two degenerate ground states of the antiferromagnet—shown in Fig. 3(b)—we used resonant scattering calculations. The resonant scattering amplitude from the n th scatterer in a magnetic system is usually expressed to first order in magnetization using the electric-dipole approximation:

$$f_n = f_0(E)\vec{\epsilon}'^* \cdot \vec{\epsilon} - if_1(E)(\vec{\epsilon}'^* \times \vec{\epsilon}) \cdot \vec{m}_n, \quad (2)$$

where f_0 and f_1 are energy-dependent constants, $\vec{\epsilon}'$ and $\vec{\epsilon}$ are the polarization of the scattered and incident x rays, respectively, and \vec{m}_n is the magnetization direction. The intensity I of scattering is equal to the sum over all scatterers:

$$I = \left| \sum_n f_n e^{i\vec{q} \cdot \vec{r}_n} \right|^2, \quad (3)$$

where \vec{q} is the scattering vector ($\vec{q} = \vec{k}' - \vec{k}$) and \vec{r}_n is the position of the n th scatterer.

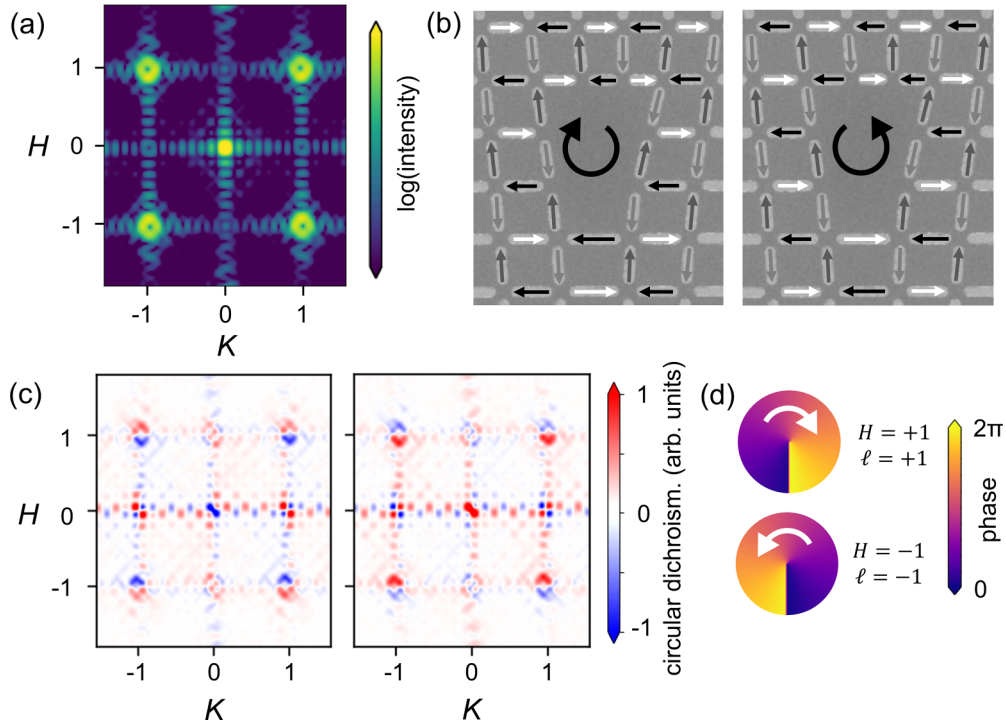


FIG. 3. Resonant x-ray scattering calculations. (a) Calculated diffraction from the artificial antiferromagnet with a \mathbb{Z}_2 defect. (b) The two possible ground states ($\mathbb{Z}_m = \pm 1$) overlaid on an SEM image. (c) Simulated circular dichroism patterns corresponding to the configurations in (b). (d) Phase of the beams for $H = \pm 1$. The direction of the phase gradient (white arrows) interacts differently with the magnetic defect configurations, giving rise to distinct asymmetry patterns.

Scattering from the $10 \times 10 \mu\text{m}^2$ nanomagnet array was calculated [58]. The resulting intensity profile is shown in Fig. 3(a) for the sum of right- and left-circularly polarized incident x rays. The experimental scattering pattern is reproduced well, with OAM beams with a central dark spot due to the phase singularity appearing at the expected (H, K) values. Differences between the experimental and theoretical peak shape are due to additional interference effects that arise from the coherent x rays used in the experiment [58].

Next, we calculated the difference in scattered intensity for right- or left-circularly polarized incident x rays. We simulated the two possible magnetic ground states, as shown in Fig. 3(b), with defects of topological charge $\mathbb{Z}_m = \pm 1$. Figure 3(c) shows the resulting circular dichroism. The $\mathbb{Z}_m = +1$ configuration matches the experimentally observed pattern in Fig. 2(b). The pattern reverses for $\mathbb{Z}_m = -1$, showing that this can be used to distinguish between two antiferromagnetic ground states. This also reproduces the circular dichroism observed previously for a different scattering geometry [34,58].

The phases of the scattered OAM beams at $H = \pm 1$ are shown in Fig. 3(d). Considering the $H = +1$ peak, we can see the relationship between the dichroism and the winding magnetization around the defect. When the defect winds in the same (opposite) direction as the OAM phase, the right-circularly polarized beam is scattered preferentially down (up), and similarly the left-circularly polarized beam is scattered preferentially up (down), giving rise to the dichroism patterns in Fig. 3(c).

The two ground states are degenerate, so they should form with equal probability if the antiferromagnet is heated above T_N and returned to room temperature. After cooling, a flip of the dichroism would indicate a change in ground state. To test this, we performed sequential measurements on an artificial antiferromagnet after heating to 380 K and cooling back to room temperature. As shown in Fig. 4, the room-temperature dichroism forms in both configurations with about 50-50 probability, which is expected for random thermal switching between two degenerate ground states.

The helicity-dependent circular dichroism that we report here can be observed if the scattering pattern is spatially resolved at the detector. The integrated intensity of an antiferromagnetic Bragg peak is the same for right- and left-circularly polarized light. Thus, our result is consistent with polarization-dependent resonant scattering. As anticipated, it is difficult to study antiferromagnetic domains due to their zero net magnetization, particularly in the case of phase domains where the order parameter remains the same, but the phase is shifted by 180 degrees [19]. For the case of scattering from the artificial antiferromagnet presented here, helicity-dependent circular dichroism in the scattered OAM beam can determine the real-space antiferromagnetic configuration. It is likely that with a beam size smaller than antiferromagnetic domains, it will be possible to determine the precise ground state by measuring the phase dichroism. Furthermore, in coherent diffraction where a speckle pattern is present, the phase dichroism could be used to differentiate domain structures that are geometrically identical, but opposite in phase.

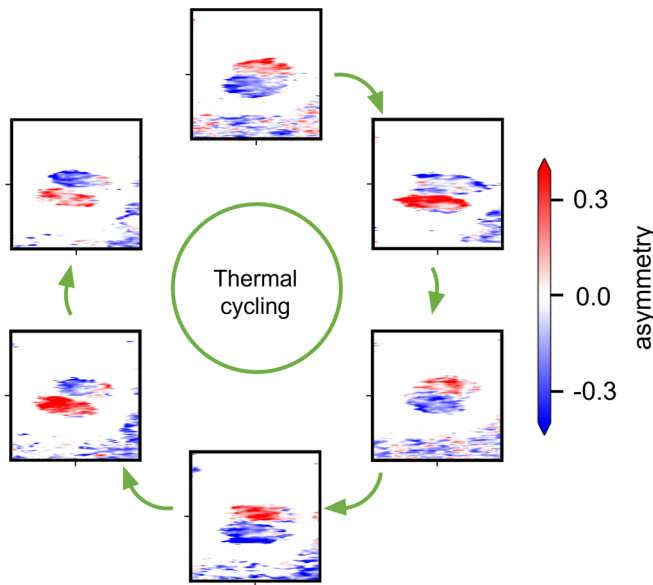


FIG. 4. Changing the antiferromagnetic ground state. The $(H, K) = (1, -1)$ peak is shown. When heated to 380 K and cooled back to room temperature, one of two antiferromagnetic ground states randomly forms. The room-temperature dichroism is shown after each of six subsequent thermal cycles.

In our experiment, complete understanding of an antiferromagnetic ground state configuration implies we can access sufficient information to characterize the specific antiferromagnetic sublattices (i.e., where magnetization is parallel, antiparallel, or perpendicular to the x-ray beam), which could lead to new techniques for imaging antiferromagnetic domains. A promising future avenue will be to first create an OAM beam and then use it to measure resonant diffraction from a traditional antiferromagnet. Given the small size of the incident OAM beam, it is also naturally suited for nanodiffraction applications, where it could identify domain walls, chiral defects, or topological defects. Furthermore, if an OAM beam can be used to measure specific spin sublattices, it could also be used as a direct method for measuring spin currents.

Finally, an analogy can be drawn to the photonic spin Hall effect (PSHE). The PSHE describes photons with different circular polarizations (i.e., photons with opposite spin angular momenta) displaced in opposite directions after interacting with a medium with inhomogeneous refractive index. For the PSHE, the photons and spatially varying refractive index play a role similar to charge carriers and the electric potential gradient in the ordinary Hall effect. Experiments demonstrating the PSHE often use metamaterials (structures engineered to have properties different than those of the constituent material) to study this spin-orbit interaction of light [59–62]. In the present case, our artificial antiferromagnet also acts as a metamaterial, and the interplay between spin and orbital angular momentum leads to a process where different circular polarizations are scattered asymmetrically.

This work was supported by the Laboratory Directed Research and Development Program of Lawrence Berkeley National Laboratory under U.S. Department of Energy Contract No. DE-AC02-05CH11231. This work used the Timepix-based soft x-ray detector, development of which is supported by DOE through award RoyTimepixDetector. This research used resources of the Advanced Light Source, a U.S. DOE Office of Science User Facility under Contract No. DE-AC02-05CH11231. Work at the Molecular Foundry was supported by the Office of Science, Office of Basic Energy Sciences, of the U.S. Department of Energy under Contract No. DE-AC02-05CH11231. Work performed at the Center for Nanoscale Materials, a U.S. Department of Energy Office of Science User Facility, was supported by the U.S. DOE, Office of Basic Energy Sciences, under Contract No. DE-AC02-06CH11357. The work is supported by the U.S. Department of Energy, Office of Science, Office of Basic Energy Sciences, under Award No. DE-SC0016519. This work was performed in part at the University of Kentucky Center for Nanoscale Science and Engineering, Electron Microscopy Center, and Center for Advanced Materials, members of the National Nanotechnology Coordinated Infrastructure (NNCI), which is supported by the National Science Foundation (Grant No. NNCI-2025075).

- [1] Y. L. Wang, G. Fabbris, D. Meyers, N. H. Sung, R. E. Baumbach, E. D. Bauer, P. J. Ryan, J.-W. Kim, X. Liu, M. P. M. Dean, G. Kotliar, and X. Dai, *Phys. Rev. B* **96**, 085146 (2017).
- [2] R. Misawa, H. Ueda, K. Kimura, Y. Tanaka, and T. Kimura, *Phys. Rev. B* **103**, 174409 (2021).
- [3] T. Matsumura, H. Nakao, and Y. Murakami, *J. Phys. Soc. Jpn.* **82**, 021007 (2013).
- [4] V. Scagnoli and S. W. Lovesey, *Phys. Rev. B* **79**, 035111 (2009).
- [5] J. Fernández-Rodríguez, V. Scagnoli, C. Mazzoli, F. Fabrizi, S. W. Lovesey, J. A. Blanco, D. S. Sivia, K. S. Knight, F. de Bergevin, and L. Paolasini, *Phys. Rev. B* **81**, 085107 (2010).
- [6] R. Comin and A. Damascelli, *Annu. Rev. Condens. Matter Phys.* **7**, 369 (2016).
- [7] L. Paolasini and F. de Bergevin, *C. R. Phys.* **9**, 550 (2008).
- [8] Y. Murakami and S. Ishihara, *Resonant X-Ray Scattering in Correlated Systems* (Springer, Berlin, Heidelberg, 2017).
- [9] S. Hwan Chun, J.-W. Kim, J. Kim, H. Zheng, C. C. Stoumpos, C. D. Malliakas, J. F. Mitchell, K. Mehlawat, Y. Singh, Y. Choi *et al.*, *Nat. Phys.* **11**, 462 (2015).
- [10] B. Keimer and J. E. Moore, *Nat. Phys.* **13**, 1045 (2017).
- [11] Y. Yamasaki, H. Nakao, and T.-h. Arima, *J. Phys. Soc. Jpn.* **89**, 083703 (2020).
- [12] N. Sasabe, M. Kimata, and T. Nakamura, *Phys. Rev. Lett.* **126**, 157402 (2021).
- [13] G. van der Laan, *Phys. Rev. B* **104**, 094414 (2021).
- [14] S. Sakamoto, T. Higo, M. Shiga, K. Amemiya, S. Nakatsuji, and S. Miwa, *Phys. Rev. B* **104**, 134431 (2021).

- [15] R. D. Johnson, P. Barone, A. Bombardi, R. J. Bean, S. Picozzi, P. G. Radaelli, Y. S. Oh, S.-W. Cheong, and L. C. Chapon, *Phys. Rev. Lett.* **110**, 217206 (2013).
- [16] H. Ueda, Y. Tanaka, Y. Wakabayashi, and T. Kimura, *Phys. Rev. B* **98**, 134415 (2018).
- [17] J.-Y. Chauleau, T. Chirac, S. Fusil, V. Garcia, W. Akhtar, J. Tranchida, P. Thibaudeau, I. Gross, C. Blouzon, A. Finco *et al.*, *Nat. Mater.* **19**, 386 (2020).
- [18] C. Léveillé, S. Flewett, E. Burgos-Parra, Y. Sassi, W. Legrand, F. Ajejas, V. Cros, N. Reyren, and N. Jaouen, *Phys. Rev. B* **104**, L060402 (2021).
- [19] S.-W. Cheong, M. Fiebig, W. Wu, L. Chapon, and V. Kiryukhin, *npj Quantum Mater.* **5**, 3 (2020).
- [20] A. Rodríguez-Fernández, J. A. Blanco, S. W. Lovesey, V. Scagnoli, U. Staub, H. C. Walker, D. K. Shukla, and J. Stempfer, *Phys. Rev. B* **88**, 094437 (2013).
- [21] M. J. Padgett, *Opt. Express* **25**, 11265 (2017).
- [22] X. Wang, Z. Nie, Y. Liang, J. Wang, T. Li, and B. Jia, *Nanophotonics* **7**, 1533 (2018).
- [23] R. Chen, H. Zhou, M. Moretti, X. Wang, and J. Li, *IEEE Commun. Surv. Tutorials* **22**, 840 (2019).
- [24] D. M. Fatkhiyev, M. A. Butt, E. P. Grakhova, R. V. Kutluyarov, I. V. Stepanov, N. L. Kazanskiy, S. N. Khonina, V. S. Lyubopytov, and A. K. Sultanov, *Sensors* **21**, 4988 (2021).
- [25] K. Dholakia and T. Čížmár, *Nat. Photonics* **5**, 335 (2011).
- [26] L. Li and F. Li, *Phys. Rev. E* **88**, 033205 (2013).
- [27] R. W. Heeres and V. Zwiller, *Nano Lett.* **14**, 4598 (2014).
- [28] L. Rego, K. M. Dorney, N. J. Brooks, Q. L. Nguyen, C.-T. Liao, J. San Román, D. E. Couch, A. Liu, E. Pisanty, M. Lewenstein *et al.*, *Science* **364**, eaaw9486 (2019).
- [29] J. B. Rosenzweig, *Nat. Photonics* **13**, 141 (2019).
- [30] Y. Ishii, K. Yamamoto, Y. Yokoyama, M. Mizumaki, H. Nakao, T.-h. Arima, and Y. Yamasaki, *Phys. Rev. Appl.* **14**, 064069 (2020).
- [31] Y. Ishii, H. Nakao, M. Mizumaki, Y. Wakabayashi, T.-h. Arima, and Y. Yamasaki, *Sci. Rep.* **12**, 1044 (2022).
- [32] J. R. Rouxel, B. Rösner, D. Karpov, C. Bacellar, G. F. Mancini, F. Zinna, D. Kinschel, O. Cannelli, M. Oppermann, C. Svetina *et al.*, *Nat. Photonics* **16**, 570 (2022).
- [33] J. C. T. Lee, S. J. Alexander, S. D. Kevan, S. Roy, and B. J. McMorran, *Nat. Photonics* **13**, 205 (2019).
- [34] J. S. Woods, X. M. Chen, R. V. Chopdekar, B. Farmer, C. Mazzoli, R. Koch, A. S. Tremsin, W. Hu, A. Scholl, S. Kevan, S. Wilkins, W. K. Kwok, L. E. De Long, S. Roy, and J. T. Hastings, *Phys. Rev. Lett.* **126**, 117201 (2021).
- [35] L. Loetgering, M. Baluktsian, K. Keskinbora, R. Horstmeyer, T. Wilhein, G. Schütz, K. S. Eikema, and S. Witte, *Sci. Adv.* **6**, eaax8836 (2020).
- [36] Y. Takahashi, A. Suzuki, S. Furutaku, K. Yamauchi, Y. Kohmura, and T. Ishikawa, *Phys. Rev. B* **87**, 121201(R) (2013).
- [37] Y. Taira and Y. Kohmura, *J. Opt.* **21**, 045604 (2019).
- [38] A. Sakdinawat and Y. Liu, *Opt. Lett.* **32**, 2635 (2007).
- [39] M. van Veenendaal and I. McNulty, *Phys. Rev. Lett.* **98**, 157401 (2007).
- [40] K. A. Forbes and D. L. Andrews, *Phys. Rev. Res.* **1**, 033080 (2019).
- [41] K. A. Forbes and D. L. Andrews, *J. Phys. Photonics* **3**, 022007 (2021).
- [42] L. Ye, J. R. Rouxel, S. Asban, B. Rösner, and S. Mukamel, *J. Chem. Theory Comput.* **15**, 4180 (2019).
- [43] M. Fanciulli, M. Pancaldi, E. Pedersoli, M. Vimal, D. Breteau, M. Luttmann, D. De Angelis, P. R. Ribič, B. Rösner, C. David, C. Spezzani, M. Manfredda, R. Sousa, I. L. Prejbeanu, L. Vila, B. Dieny, G. DeNinno, F. Capotondi, M. Sacchi, and T. Ruchon, *Phys. Rev. Lett.* **128**, 077401 (2022).
- [44] G. De Ninno, J. Wätzel, P. R. Ribič, E. Allaria, M. Coreno, M. B. Danailov, C. David, A. Demidovich, M. Di Fraia, L. Giannessi *et al.*, *Nat. Photonics* **14**, 554 (2020).
- [45] J. Wätzel, P. R. Ribič, M. Coreno, M. B. Danailov, C. David, A. Demidovich, M. Di Fraia, L. Giannessi, K. Hansen, Š. Krušič, M. Manfredda, M. Meyer, A. Mihelič, N. Mirian, O. Plekan, B. Ressel, B. Rösner, A. Simoncig, S. Spampinati, M. Stupar, M. Žitnik, M. Zangrando, C. Callegari, J. Brakdar, and G. De Ninno, *Phys. Rev. Lett.* **128**, 157205 (2022).
- [46] M. van Veenendaal, *Phys. Rev. B* **92**, 245116 (2015).
- [47] S. H. Skjærvø, C. H. Marrows, R. L. Stamps, and L. J. Heyderman, *Nat. Rev. Phys.* **2**, 13 (2020).
- [48] P. Schiffer and C. Nisoli, *Appl. Phys. Lett.* **118**, 110501 (2021).
- [49] A. Farhan, P. M. Derlet, A. Kleibert, A. Balan, R. V. Chopdekar, M. Wyss, J. Perron, A. Scholl, F. Nolting, and L. J. Heyderman, *Phys. Rev. Lett.* **111**, 057204 (2013).
- [50] V. Kapaklis, U. B. Arnalds, A. Farhan, R. V. Chopdekar, A. Balan, A. Scholl, L. J. Heyderman, and B. Hjörvarsson, *Nat. Nanotechnol.* **9**, 514 (2014).
- [51] S. A. Morley, D. Alba Venero, J. M. Porro, S. T. Riley, A. Stein, P. Steadman, R. L. Stamps, S. Langridge, and C. H. Marrows, *Phys. Rev. B* **95**, 104422 (2017).
- [52] X. M. Chen, B. Farmer, J. S. Woods, S. Dhuey, W. Hu, C. Mazzoli, S. B. Wilkins, R. V. Chopdekar, A. Scholl, I. K. Robinson, L. E. DeLong, S. Roy, and J. T. Hastings, *Phys. Rev. Lett.* **123**, 197202 (2019).
- [53] S. Lendinez and M. B. Jungfleisch, *J. Phys.: Condens. Matter* **32**, 013001 (2020).
- [54] S. Gliga, E. Iacocca, and O. G. Heinonen, *APL Mater.* **8**, 040911 (2020).
- [55] M. T. Kaffash, S. Lendinez, and M. B. Jungfleisch, *Phys. Lett. A* **402**, 127364 (2021).
- [56] J. Perron, L. Anghinolfi, B. Tudu, N. Jaouen, J.-M. Tonnerre, M. Sacchi, F. Nolting, J. Lüning, and L. J. Heyderman, *Phys. Rev. B* **88**, 214424 (2013).
- [57] D. Sung, C. Jung, B.-G. Cho, W. Jo, H.-S. Han, K.-S. Lee, V. Bhat, B. Farmer, L. De Long, K. B. Lee *et al.*, *Nanoscale* **10**, 13159 (2018).
- [58] See Supplemental Material at <http://link.aps.org/supplemental/10.1103/PhysRevB.107.L060407> for (S1) details about materials fabrication and experimental methods; (S2) details of XMCD PEEM; (S3) details on resonant scattering calculations; (S4) details about coherent diffraction effects on the scattered beam; (S5) resonant scattering calculations using another diffraction geometry; and (S6) data from a defect-free antiferromagnet. The Supplemental Material includes Refs. [63–70].
- [59] X. Yin, Z. Ye, J. Rho, Y. Wang, and X. Zhang, *Science* **339**, 1405 (2013).
- [60] W. Luo, S. Xiao, Q. He, S. Sun, and L. Zhou, *Adv. Opt. Mater.* **3**, 1102 (2015).
- [61] Y. Liu, Y. Ke, H. Luo, and S. Wen, *Nanophotonics* **6**, 51 (2017).
- [62] X. Ling, X. Zhou, K. Huang, Y. Liu, C.-W. Qiu, H. Luo, and S. Wen, *Rep. Prog. Phys.* **80**, 066401 (2017).
- [63] A. S. Tremsin, J. V. Vallergera, and R. R. Raffanti, *J. Instrum.* **13**, C11005 (2018).

- [64] A. S. Tremsin, J. V. Vallerga, and O. H. W. Siegmund, *Nucl. Instrum. Methods Phys. Res., Sect. A* **949**, 162768 (2020).
- [65] A. S. Tremsin, J. V. Vallerga, O. H. W. Siegmund, J. Woods, L. E. De Long, J. T. Hastings, R. J. Koch, S. A. Morley, Y.-D. Chuang, and S. Roy, *J. Synchrotron Radiat.* **28**, 1069 (2021).
- [66] J. Fink, E. Schierle, E. Weschke, and J. Geck, *Rep. Prog. Phys.* **76**, 056502 (2013).
- [67] Y. Tanaka, T. Kojima, Y. Takata, A. Chainani, S. W. Lovesey, K. S. Knight, T. Takeuchi, M. Oura, Y. Senba, H. Ohashi, and S. Shin, *Phys. Rev. B* **81**, 144104 (2010).
- [68] S. Zheng and J. Wang, *Sci. Rep.* **7**, 40781 (2017).
- [69] V. V. Kotlyar, A. A. Kovalev, and A. P. Porfirev, *Opt. Express* **27**, 11236 (2019).
- [70] K. Dai, C. Gao, L. Zhong, Q. Na, and Q. Wang, *Opt. Lett.* **40**, 562 (2015).